

REVIEW

Open Access



High-speed Si-Ge avalanche photodiodes

Binhao Wang^{1,2*}  and Jifang Mu³

*Correspondence:

wangbinhao@opt.ac.cn

¹State Key Laboratory of Transient Optics and Photonics, Xi'an Institute of Optics and Precision Mechanics, Chinese Academy of Sciences, Xi'an, China

Full list of author information is available at the end of the article

Abstract

High-speed optical interconnects of data centers and high performance computers (HPC) have become the rapid development direction in the field of optical communication owing to the explosive growth of market demand. Currently, optical interconnect systems are moving towards higher capacity and integration. High-sensitivity receivers with avalanche photodiodes (APDs) are paid more attention due to the capability to enhance gain bandwidth. The impact ionization coefficient ratio is one crucial parameter for avalanche photodiode optimization, which significantly affects the excess noise and the gain bandwidth product (GBP). The development of silicon-germanium (Si-Ge) APDs are promising thanks to the low impact ionization coefficient ratio of silicon, the simple structure, and the CMOS compatible process. Separate absorption charge multiplication (SACM) structures are typically adopted in Si-Ge APDs to achieve high bandwidth and low noise. This paper reviews design and optimization in high-speed Si-Ge APDs, including advanced APD structures, APD modeling and APD receivers.

Keywords: Avalanche photodiode, Photodetector, Optical interconnect, Data communication

Introduction

The emerging applications in artificial intelligence (AI), internet of things (IoT), cloud computing and storage, and video streaming result in huge demands for data communications, which have been driving the development of 5G communication, hyper-scale data centers, and exascale high performance computers (HPC). Compared to conventional copper based interconnects, optical interconnects possess properties of higher bandwidth and longer transmission distance, alleviating the crowded data traffic. Optical interconnect systems can proceed at the speed of light with multiple optical technologies, such as wavelength division multiplexing (WDM) [1–3] and mode division multiplexing (MDM) [4–7], to meet the requirements in latency and bandwidth. The development trend is towards higher integration for higher bandwidth density and lower cost per gigabit. Silicon photonics is a promising technology that has been widely used for applications in optical communication [8, 9], optical switch [10, 11], optical computing [12, 13], light detection and ranging (LIDAR) [14, 15], optical sensing [16–18], and so on and

so forth. Due to the complementary metal-oxide-semiconductor (CMOS) compatible process and the high integration capability, silicon photonics has shown superior performance in aforementioned applications. After decades of development, basic silicon photonic devices, including waveguides, couplers, phase shifters, modulators, and photodiodes, are relatively mature [19–23]. The integration of light sources on silicon was the main challenge due to the indirect bandgap of silicon. Fortunately, heterogeneous bonding and heteroepitaxial technologies are promising to realize laser diodes (LDs) or semiconductor optical amplifiers (SOAs) on silicon [24–30]. As main optical components on silicon can be realized, silicon photonics is moving towards programmable or reconfigurable photonic integrated circuits (PICs) [31–33]. Recent progresses in the monolithic integration of silicon photonics and CMOS circuits show the potential of the silicon based optoelectronic technology [34–36].

Admittedly, the performance of silicon photonic devices still need to be improved. High-performance photonic devices are essential for large-scale PICs. Photodetectors for converting optical signals into electrical signals are important components in many applications. However, silicon photodetectors have low absorption coefficients at wavelengths greater than 1100 nm due to the large bandgap induced transparency. To enable silicon photonics for wide applications in O-band and C-band optical communications, the epitaxial growth of Ge on Si technology overcomes the 4.2% lattice mismatch between Si and Ge, realizing efficient light absorption for photodetection [37–39]. The bandwidth of optical interconnect systems has been doubling every 2-3 years driven by the demand of datacom. The link budget and power budget become harder to satisfy while increasing the bandwidth density in optical interconnects. High-sensitivity receivers are required for further increase in bandwidth [40, 41]. However, conventional p-i-n photodiodes are challenging to meet the demands in an optical interconnect system. Avalanche photodiodes (APDs) with internal gain can significantly increase the receiver sensitivity to relax the bandwidth requirements of optics and electronics as well as link and power budgets [42–45].

The avalanche effect not only results in multiplication gain but also generates excess noise [46, 47]. The benefit of APDs strongly depends on whether they have sufficient gain-bandwidth, which is tied closely to excess noise. The excess noise factor is strongly related to the impact ionization coefficient ratio, k [46]. Therefore, how to design an APD with a low impact ionization coefficient ratio is critical. III-V material based APDs have been investigated for decades [48–51]. Selecting a semiconductor material with favorable impact ionization coefficients is one method to realize high-performance APDs [48, 49]. Another method utilizes impact ionization engineering with desired heterostructures [50, 51]. Despite it is flexible to choose epitaxial materials, high-performance III-V APDs require complex heterostructures and lack the capability to integrate with other photonic devices. Compared to most III-V APDs, Si-Ge APDs have simpler structures and lower excess noise thanks to the extremely low impact ionization coefficient ratio in silicon [52, 53].

Typically, accurate process design kits (PDK) including transistor models are required for integrated circuit (IC) design. Similarly, compact photonic device models are also helpful for large-scale PIC design [54]. Active photonic device models with electrical and optical dynamics can strongly benefit the design of high-speed transceiver circuits [55–65]. Compared to p-i-n photodiode receivers, APD receivers require more complex

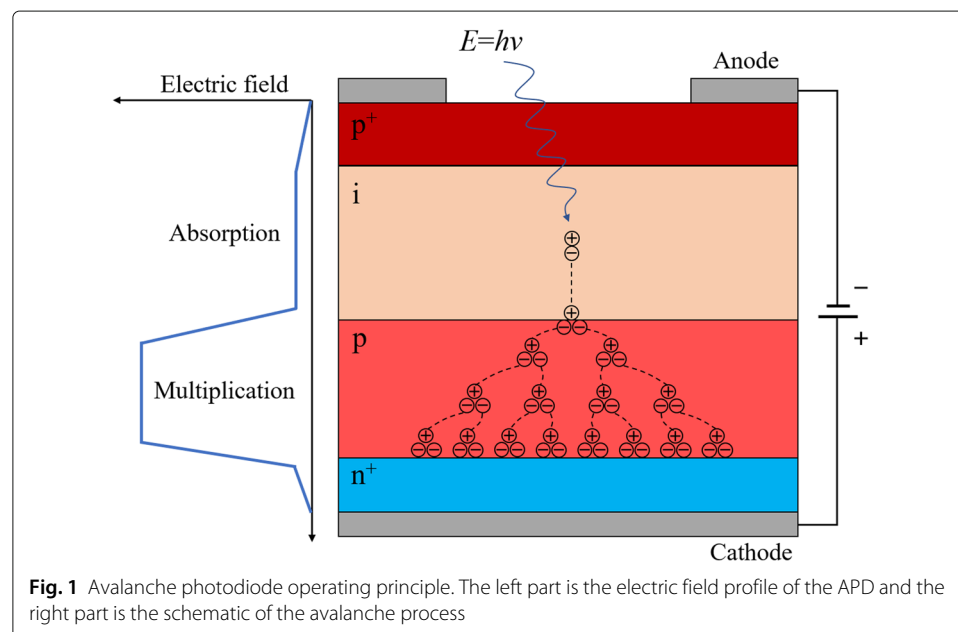
bias circuits due to the bias-dependent multiplication gain of APDs and the required high bias voltage. An accurate APD model for codesign of optical receivers is necessary [61–65]. As discussed, using APDs can improve the optical receiver sensitivity. In fact, both APD and receiver circuitry contribute to the overall noise of APD receivers, and the APD noise is a function of its multiplication gain. Thus, it is necessary to analyze the APD receiver sensitivity to find out the optimum gain region for operation [40]. This paper will review recent advances in high-speed Si-Ge APDs. The basic principles of APDs will be first described, which is followed by reviewing multiple advanced APD structures. Next, APD equivalent circuit model and the sensitivity analysis for APD receivers will be presented. Finally, the challenges and perspectives of Si-Ge APDs for applications in optical communication will be discussed.

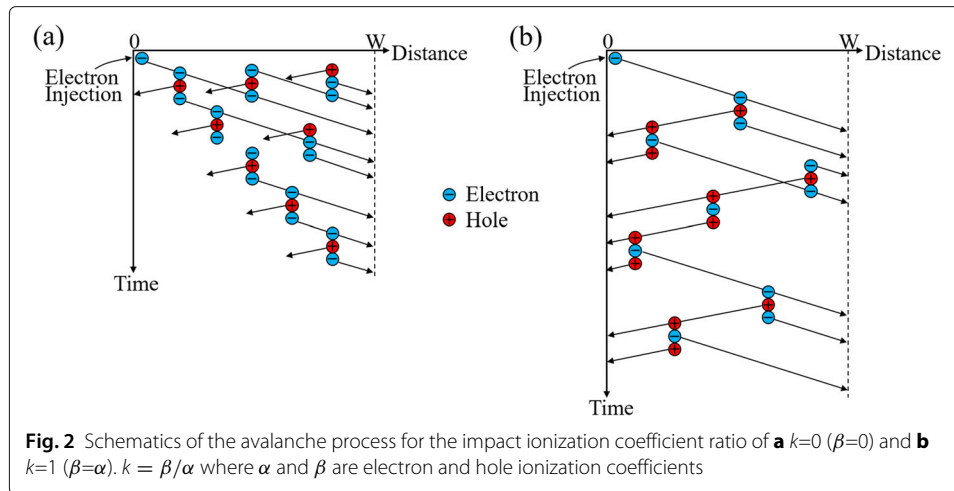
APD fundamental

The internal gain of an APD is obtained through the avalanche process, which is triggered when it is biased beyond the impact ionization threshold. Figure 1 shows the schematic of the avalanche effect occurred in an APD. The APD structure is built by simply adding a p-doping layer in a conventional p+-i-n+ photodiode [66]. The incident light is absorbed in the i-layer where electron-hole pairs are formed. Due to the low electric field in the absorption region, the carriers move to the corresponding electrodes. After these free carriers enter into the multiplication region, the high electric field speeds up their velocities, accumulating sufficient energy to excite more electrons and holes from the valence band into the conduction band. As the avalanche process illustrated in Fig. 1, a creasing number of free carriers are generated in the multiplication region.

APDs are favored due to their internal gain. However, APDs also generate excess noise along with multiplication gain, contributing to the photocurrent shot noise. The APD excess noise factor is a function of gain which is given by

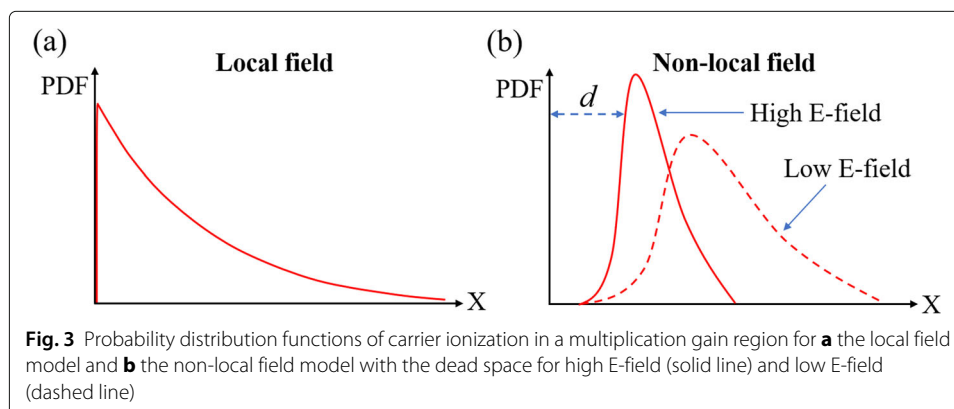
$$F(M) = k \cdot M + (1 - k)(2 - 1/M), \quad (1)$$





where k is the impact ionization coefficient ratio and M is the multiplication gain [46, 47]. The ratio k is determined by $k = \beta/\alpha$, where α and β are electron and hole ionization coefficients of the semiconductor material in multiplication region, respectively [45]. In other words, $1/\alpha$ or $1/\beta$ is the average distance of an electron or hole travelling before impact ionization. As one can find out from Eq. 1, the smaller impact ionization coefficient ratio k results in lower excess noise factor F . Figure 2 shows the avalanche process for $k = 0$ ($\beta=0$) and $k = 1$ ($\alpha=\beta$). The avalanche process for $k = 1$ is a chain-like. If an impact ionization event does not occur, it will result in much larger gain variation than for the case of $k = 0$. Therefore, the resulted excess noise for APDs with $k = 1$ is larger than the ones with $k = 0$. The impact ionization coefficient ratio k also affects APD gain-bandwidth product (GBP) [45]. For $k = 1$, both electrons and holes involve in the avalanche process that two types of carriers travel back and forth across the multiplication region. By contrast, only one transit by electrons is required for $k = 0$, which takes much shorter time to achieve the same gain. The required time for APDs to build up a certain gain is called avalanche buildup time or multiplication time, which is inversely proportional to GBP.

Equation 1 is derived based on a local-field model that the impact ionization coefficients are in local equilibrium [46]. This model can well describe the avalanche effect and excess noise when the multiplication region is thick. As shown in Fig. 3(a), the ionization probability for carriers in the multiplication region is decreased exponentially with



the distance from the injection point. However, the local-field model does not agree with the evidence that the excess noise becomes lower when thinning the multiplication layer to submicron [67, 68]. A non-local effect in the impact ionization process has been proposed to explain the phenomenon [69, 70]. As shown in Fig. 3(b), the carriers entered into the multiplication region are “cool” at the beginning and the ionization occurs only after traveling a certain distance to obtain sufficient energy. The distance d for carriers to reach the ionizing threshold, as shown in Fig. 3(b), is called “dead space” [69, 71]. To take the dead space into account, the probability distribution function (PDF) of the impact ionization are corrected as the lines shown in Fig. 3(b). When the multiplication layer is thin, the electric field needs to be higher than expected to achieve a certain multiplication gain. The width of the PDF is narrower after considering the dead space, resulting in a more deterministic ionization process. Therefore, the excess noise can be lowered by thinning the multiplication layer.

Si-Ge APD

Important performance metrics of APDs include breakdown voltage, dark current, quantum efficiency, multiplication gain, bandwidth, excess noise, and GBP. These APD key parameters typically have design trade-offs. For applications in high-speed optical interconnects, GBP and excess noise appear to be more important in APD design. The studies on monolithically integrated Si-Ge APDs raise great interests on APDs. Metal-semiconductor-metal (MSM), p-i-n, and SACM structures are commonly used for APD design [72–80]. The low bandgap of germanium results in almost the same magnitude of ionization coefficients for electrons and holes [81–84]. The impact ionization coefficient ratio k is close to 1 ($k \sim 0.9$). By contrast, the impact ionization for electrons and holes in pure silicon are quite asymmetric, yielding a k value close to 0 ($k \sim 0.02$) [82–84]. To take advantages of high absorption coefficient in germanium and low impact ionization coefficient ratio in silicon, the separate absorption charge multiplication (SACM) structure is often used in Si-Ge APD design, where a low electric field is retained in germanium to keep it below the impact ionization threshold and a high electric field is confined in silicon to trigger the ionization effect [72–74]. This design has shown superior performance in aspects of GBP and excess noise. Also, Si-Ge SACM APDs have been demonstrated with high temperature stability that the bandwidth and the GBP have negligible degradation [85]. Recent advances in high-speed Si-Ge APDs will be discussed below. It is worth noting that some APD structures can be classified into multiple categories.

Vertical SACM APD

Si-Ge APDs are initially designed as discrete normal-incidence (NI) devices for applications in optical-fiber communication [72, 86–89]. Kang et al. proposed a NI Si-Ge APD with a p+-i-p-i-n+ layer structure as shown in Fig. 4(a) and (b) [72]. The layer thicknesses and doping levels of the vertical SACM APD structure can be found in Fig. 4(a). A maximum bandwidth of 11.5 GHz was measured for a 30- μm -diameter device. The bandwidth is limited by RC time constant and carrier transit time, which is similar to a p-i-n photodiode except that an APD depletion region includes depleted germanium absorption as well as silicon charge and multiplication layers. The proposed APD design achieved an effective k of 0.09 and a GBP of 340 GHz thanks to the SACM structure. However, the operating bias voltage beyond 20 V was required to realize a reasonable high gain due to

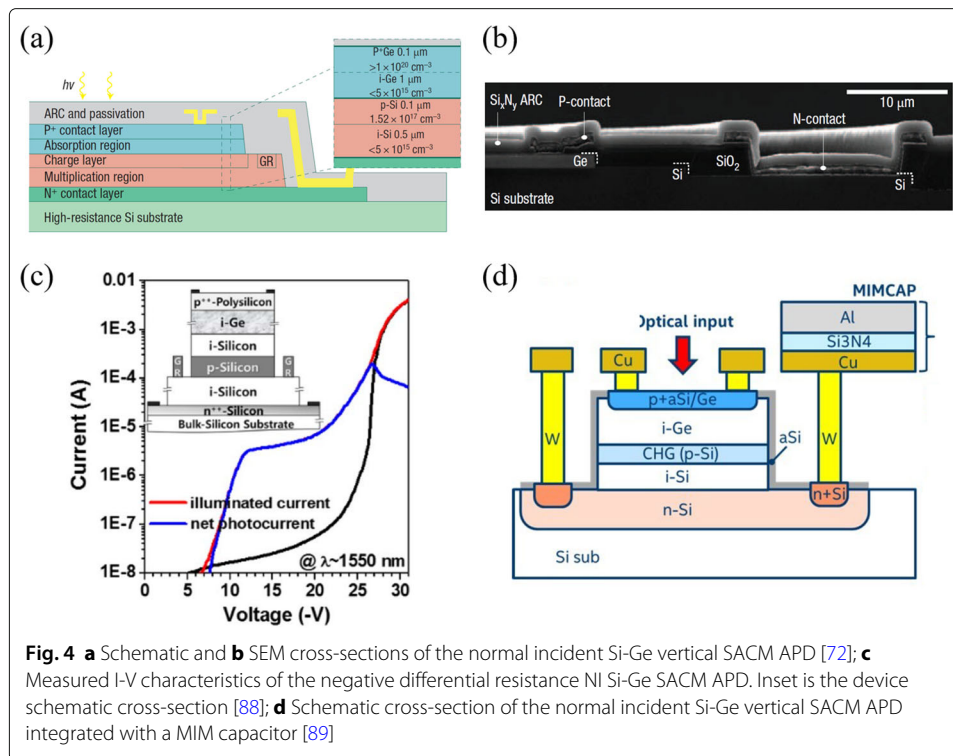


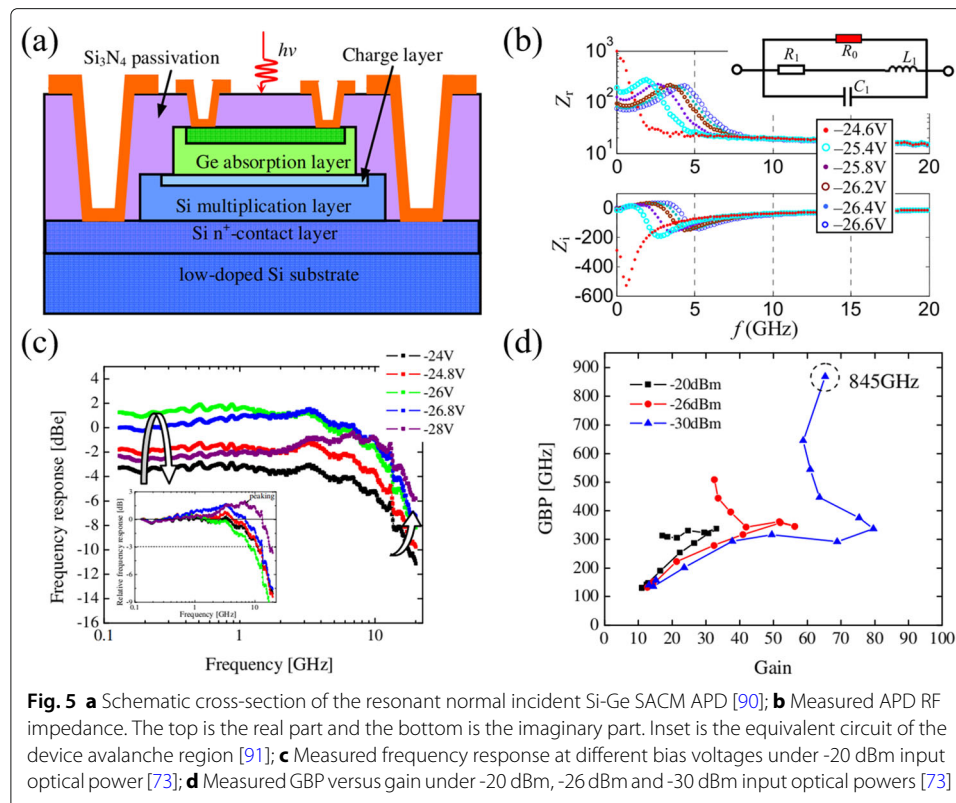
Fig. 4 **a** Schematic and **b** SEM cross-sections of the normal incident Si-Ge vertical SACM APD [72]; **c** Measured I-V characteristics of the negative differential resistance NI Si-Ge SACM APD. Inset is the device schematic cross-section [88]; **d** Schematic cross-section of the normal incident Si-Ge vertical SACM APD integrated with a MIM capacitor [89]

the thick SACM structure. The APD breakdown voltage can be reduced by thinning the SACM structure and optimizing the doping profile. Kim et al. proposed a negative differential resistance (NDR) NI SACM APD with a maximum GBP of 460 GHz as shown in the inset of Fig. 4(c) [88]. A typical I-V characteristic of the device is shown in Fig. 4(c), where the blue line is the difference between the photocurrent (red line) and the dark current (black line). It exhibited a negative photoconductance effect when the reverse bias was increased beyond reaching the maximum photocurrent.

For APD based receivers, the required high bias voltage of APDs cannot be supplied by trans-impedance amplifier (TIA) ICs directly due to the voltage limit in IC chips [89]. Typically, an APD receiver has to have an individual bypass capacitor to block the high dc bias voltage and filter out the noise from the external power supply. The required large capacitance occupies a large footprint which may not be easily integrated on a receiver IC chip owing to the restricted channel pitch in APD multi-channel applications. As shown in Fig. 4(d), Park et al. proposed a NI Si-Ge SACM APD monolithically integrated with a metal-insulator-metal (MIM) bypass capacitor [89]. The bypass capacitor was fabricated by depositing 100 nm-thick silicon nitride between copper and aluminium to realize a capacitance value of 100 pF. The responsivity of 0.21 A/W at unit gain, the bandwidth of ~20 GHz, and the GBP of 150 GHz were exhibited at 1310 nm.

Resonant SACM APD

In order to further improve the GBP, NI SACM APDs using resonant effect have been demonstrated [73, 90, 91]. Zaoui et al. proposed a resonant NI SACM APD with an ultra-high GBP of 845 GHz [73]. The schematic of the resonant APD is shown in Fig. 5(a). By designing the avalanche region properly, the real part and the imaginary part of the



APD impedance have a peak and a null at a certain frequency, respectively, as shown in Fig. 5(b). The inset in Fig. 5(b) is the equivalent circuit model of the avalanche region extracted from the curve fit of the impedance measurement [90, 91]. The resonance between the inductor and the capacitor results in a peak enhancement in the device frequency response at the high frequency range, as shown in Fig. 5(c). Figure 5(d) shows the measured GBP of the APD under different input powers. The measured highest GBP was 845 GHz at -30 dBm input optical power, corresponding to a gain of 65 and a bandwidth of 13 GHz. Although an extremely high GBP was achieved, the maximum bandwidth of the APD was still less than 20 GHz as shown in Fig. 5(c) and (d). It is well known that NI photodiodes have design trade-offs between responsivity and bandwidth. A thick germanium layer is typically grown on silicon and processed with a large surface area for sufficient light absorption, resulting in larger RC time constant and longer carrier transit time. Such trade-off can be addressed by design of waveguide coupled photodiodes to decouple light absorption and carrier collection.

Waveguide APD

Waveguide-coupled Si-Ge APDs have been demonstrated with excellent performance in terms of bandwidth, dark current and noise [74, 92–99]. The major advantage of waveguide APDs over NI APDs is that the light propagation and carrier collection paths are orthogonal to each other. More importantly, waveguide APDs are more suitable for large-scale PICs, which the incident light in silicon waveguide is evanescently coupled into germanium for absorption. Light evanescent coupling schemes for waveguide photodiodes include top-to-down, down-to-top, side-coupling, and Butt-coupling, where the

down-to-top coupling is the most common one for waveguide-coupled APDs owing to the CMOS compatible process and the simple structure. Huang et al. from Hewlett Packard Labs proposed a waveguide Si-Ge APD adopting down-to-top coupling scheme [94]. The detailed SACM structure can be found in Fig. 6(a). Unlike the p+-i-p-i-n+ SACM structure proposed in Fig. 4(a), here a p+-p-i-n+ structure with thinner layer thicknesses was designed to reduce the breakdown voltage as well as achieve high bandwidth and low noise. Figure 6(b) illustrates the electric field distribution of the waveguide Si-Ge APD at a bias voltage near the breakdown. It is clear to see that a high electric field is confined in the silicon multiplication layer. A measured maximum bandwidth of 25 GHz and a GBP of 276 GHz were demonstrated by optimizing the SACM structure. Huang et al. from SiFotonics demonstrated a waveguide SACM APD with an ultra-high bandwidth of 56 GHz at a gain of 1.8 and a bandwidth of 36 GHz at a gain of 10, as shown in Fig. 6(c) and (d), achieving promising performance of waveguide-coupled APDs as well [95]. Huang et al. from Intel proposed a recess-type waveguide-coupled SACM APD, as shown in Fig. 6(d) [99]. The silicon recess design minimized the step height between silicon waveguide and germanium absorption layers, which realized higher evanescent coupling efficiency and better mode confinement. A GBP of 260 GHz and a breakdown voltage of 16.5 V were exhibited.

APD with a reflector

The responsivity of a waveguide APD can be impacted by the epitaxial germanium thickness, the absorption length, and the evanescent coupling efficiency. The parasitic capacitance dominated by the germanium absorption and silicon multiplication area limits the APD bandwidth if the carrier transit time is negligible. In order to improve the responsivity bandwidth product, Wang et al. proposed a Si-Ge APD with a distributed Bragg reflector (DBR) as shown in Fig. 7(a) [100]. The waveguide length can be shorten

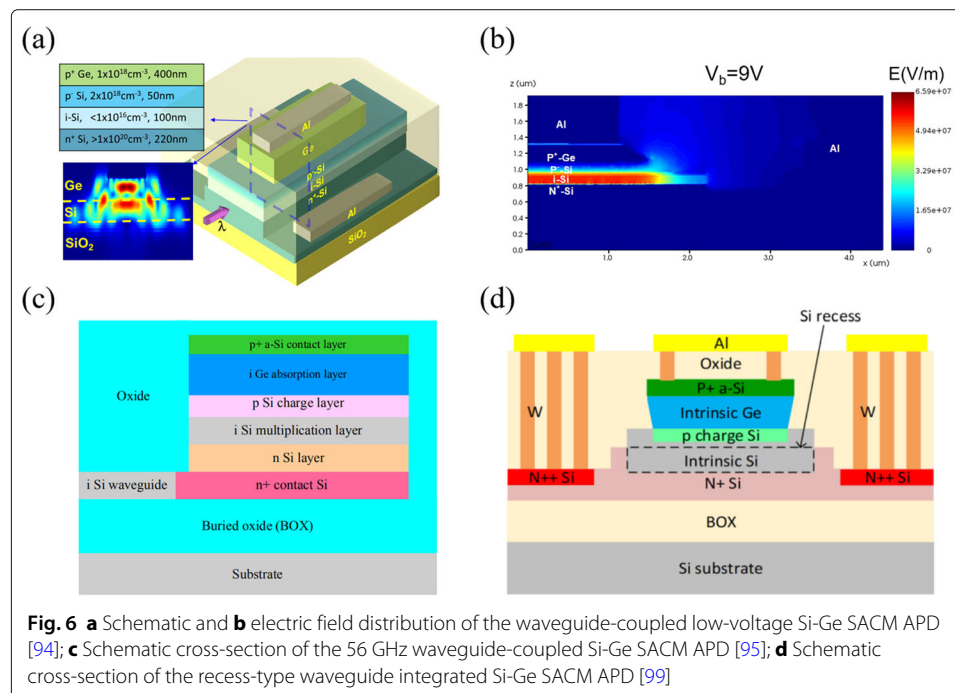
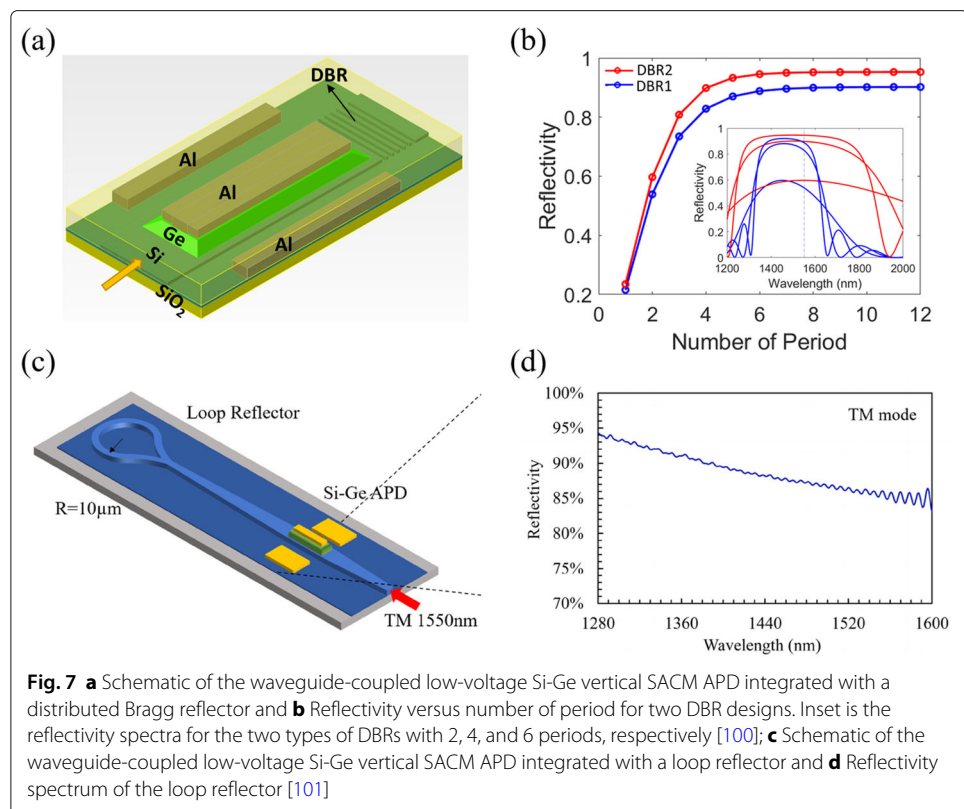


Fig. 6 **a** Schematic and **b** electric field distribution of the waveguide-coupled low-voltage Si-Ge SACM APD [94]; **c** Schematic cross-section of the 56 GHz waveguide-coupled Si-Ge SACM APD [95]; **d** Schematic cross-section of the recess-type waveguide integrated Si-Ge SACM APD [99]



with the help of DBR that the incident light is not absorbed when propagating in the waveguide will be reflected back for the second absorption. As shown in Fig. 7(b), a few number of pairs for DBR design realized a reflectivity of higher than 90%, and the inset of Fig. 7(b) indicated that the DBR design had a wide optical bandwidth. As a result, the APD quantum efficiency was improved from 60% to 90% with the assistance of DBR and the electrical bandwidth had no degradation compared to APDs without a DBR. It is worth to mention that the parameters of the DBR, such as period, fill factor, and number of pairs, have to be carefully designed to achieve high-sufficient reflectivity and meet fabrication requirements simultaneously. To relax the DBR fabrication tolerance, other types of reflectors, such as loop reflectors, are alternatives. As shown in Fig. 7(c), Yuan et al. proposed a Si-Ge waveguide APD integrated with a loop reflector at the end [101]. The loop reflector exhibited even wider optical bandwidth than DBRs, as the reflectivity spectrum shown in Fig. 7(d). Such design also improved the responsivity by around 50% without electrical bandwidth degradation. However, the size of the APD with a loop reflector is relatively large because of the need for long taper and big loop radius to achieve low light propagation loss.

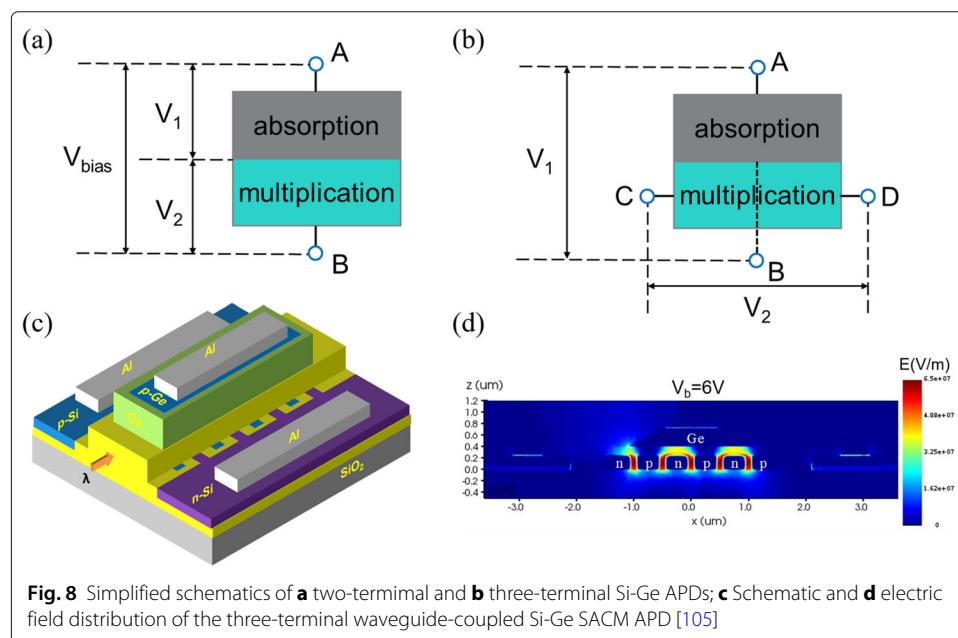
Low-voltage APD

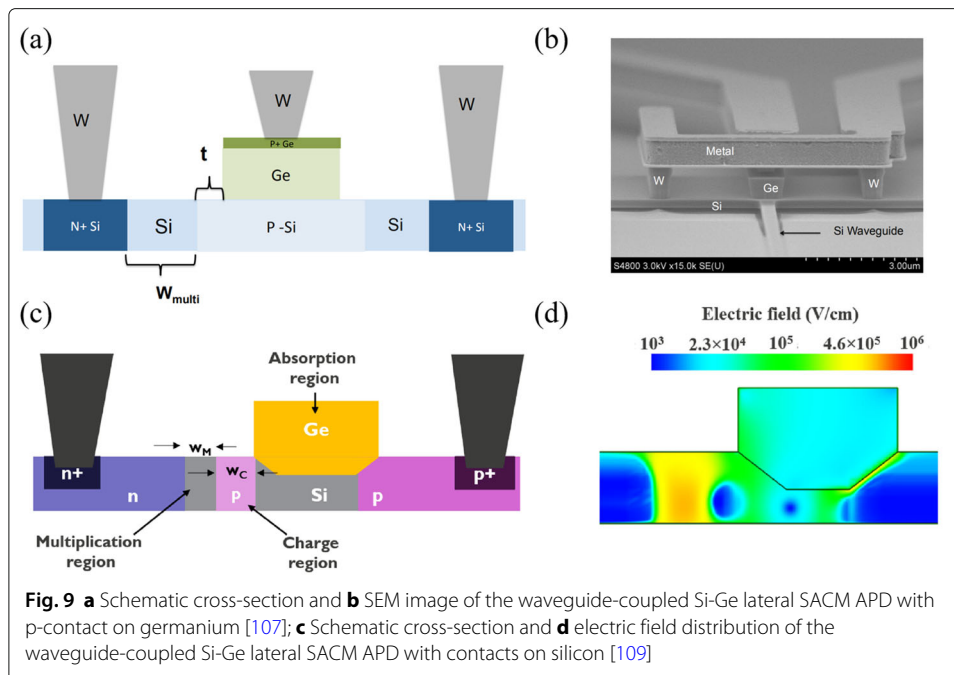
Due to the low-voltage power-rail requirements in HPC applications, Si-Ge APDs with low breakdown voltage have attracted researchers' interest [102–104]. Unlike the APD designs with high breakdown voltages at around 20 V or beyond discussed in [72, 86–88], APDs with the thin SACM structure and the optimum doping profile, as shown in Figs. 6(a, b) and 7(a, c), can achieve a breakdown voltage as low as 10 V [94, 100, 101].

For typical SACM APDs, the required bias voltage is the sum of the voltage drops in the absorption and multiplication regions because the germanium absorption and silicon multiplication regions are in series, as shown in Fig. 8(a). Design of a SACM APD with the absorption and multiplication regions in parallel can further reduce the APD bias voltage, as the simplified schematic illustrated in Fig. 8(b). Zeng et al. proposed a three-terminal Si-Ge APD with an ultra-low breakdown voltage (Fig. 8(c)) [105]. Unlike two-terminal design, three-terminal APDs can realize independent electric controls on charge and multiplication layers by two separate voltage drops. This design not only reduces the APD breakdown voltage but also relax the fabrication tolerance on the doping profile. The electric field of the proposed design is illustrated in Fig. 8(d). The high electric field confined in the finger gap was the intrinsic silicon region for multiplication. The three-terminal Si-Ge APD with a breakdown voltage of 6 V and a GBP over 280 GHz was demonstrated. Also, the design allows to use the standard CMOS process and no additional silicon epitaxial growths are required.

Lateral SACM APD

Aforementioned Si-Ge APDs adopt vertical SACM structure, which requires to epitaxially grow an additional silicon charge layer. In order to reduce the device fabrication complexity, lateral SACM APDs have been demonstrated, in which the charge and multiplication regions are on one silicon layer [106–109]. Martinez et al. proposed a lateral SACM APD with a breakdown voltage of more than 30 V and a GBP of 432 GHz as shown in Fig. 9(a) and (b). The device symmetry, including contacts, is important for field configuration considerations, which raises requirements of fabrication tolerance to achieve device performance consistence. The p-charge layer was designed to have different overlaps relative to the germanium sidewall. The higher gain in the no-overlap device was observed due to the realized higher electric field in germanium. In addition, the multiplication width was also studied with variations from 200 nm to 1000 nm. The larger

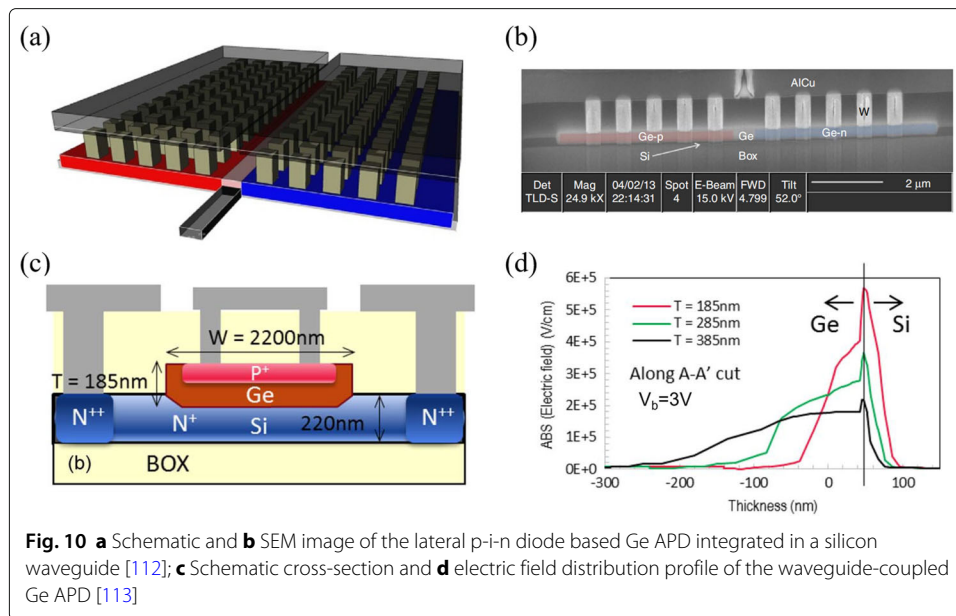




bandwidth was observed with narrower multiplication width because of the less carrier transit time. More specifically, lateral SACM APDs can be designed with contacts on silicon only that the process for contact doping on germanium is not necessary [108, 109]. Srinivasan et al. demonstrated a lateral SACM APD with a gain of 11 and a bandwidth of 27 GHz at -12 V, as shown in Fig. 9(c) [108, 109]. The device was optimized to form a high electric field in the silicon multiplication region as shown in Fig. 9(d). This design has no needs to retain the device symmetry, relaxing the fabrication tolerance. However, it requires smaller linewidths in processes, such as the narrow width of the silicon charge region. Two designs with a nominal multiplication region width of 200 nm and a doping level of around 10^{18} cm^{-3} but different charge region widths of 50 nm and 100 nm were investigated. The experimental results exhibited a trade-off between bandwidth and dark current.

Germanium APD

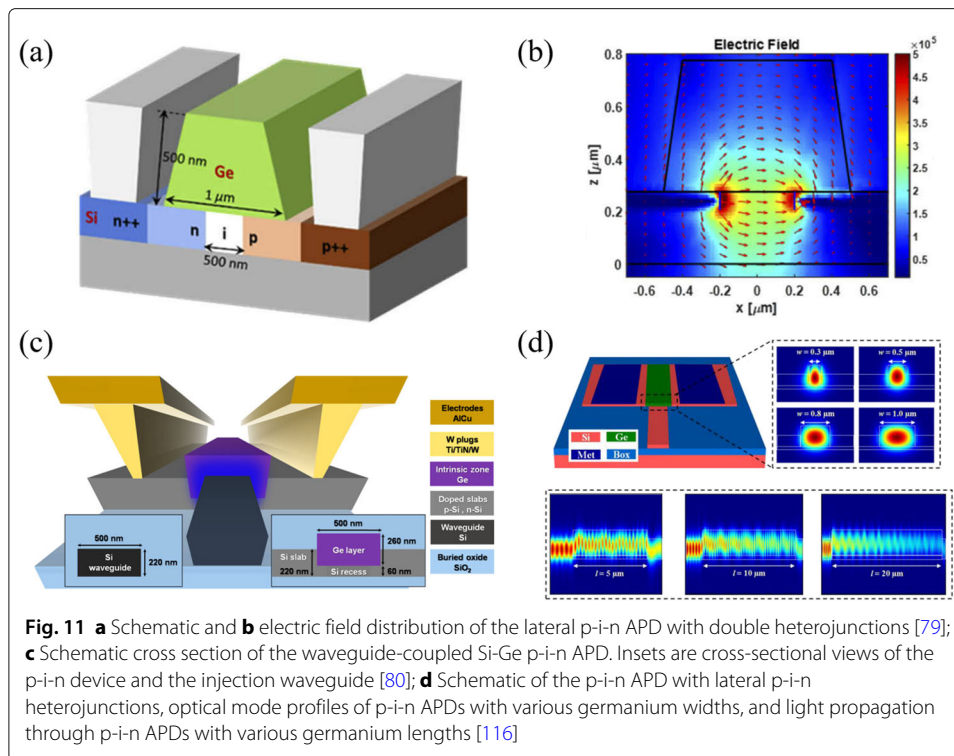
In general, germanium APDs can achieve lower breakdown voltage than Si-Ge APDs, because the required electric field to trigger the impact ionization in germanium is lower than that of silicon [110, 111]. Ge APDs with low breakdown voltages have been demonstrated in recent years [112–115]. Virot et al. demonstrated a waveguide-coupled Ge APD with a breakdown voltage of 7 V [112]. The schematic and the SEM image of the Ge APD are shown in Fig. 10(a) and (b). As mentioned before, electrons and holes have quite similar impact ionization coefficients in germanium. The excess noise factor of a Ge APD should be high because both absorption and multiplication take place in germanium. In [112], a narrow width multiplication region of 500 nm was chosen to enhance the large dead space effect, contributing to a remarkable reduction of the excess noise factor. A GBP of 193 GHz and an effective k value of 0.4 were achieved. More specifically, Chen et al. demonstrated a sub 5 V waveguide-coupled Ge APD with a GBP of 140



GHz and an effective k value of 0.2, as shown in Fig. 10(c) [113]. Ge APDs with various germanium layer thicknesses were investigated in [113]. As one can see in Fig. 10(d), the thinner germanium layer has higher electric field near the interface of Ge/Si. In [113], a 185 nm thin germanium layer was adopted for the low operating voltage where the electric field dropped sharply away from the Ge/Si interface. This design greatly suppressed the avalanche excess noise due to the limited thickness of the multiplication region. The demonstrated effective k value was much lower than the k in germanium since the avalanche effect occurred in both germanium and silicon near their interface as shown in Fig. 10(d).

p-i-n APD

SACM APDs can realize high GBP and low excess noise but require accurate control of the doping profile in SACM structure, including layer thicknesses (or silicon charge and multiplication widths for lateral SACM APDs) and doping levels. By contrast, lateral p-i-n APDs with double heterojunctions are an alternative for APD design [79, 80, 116]. Zhang et al. proposed an APD with a lateral p-i-n junction, as shown in Fig. 11(a), exhibiting a maximum responsivity of 15.2 A/W at 16x avalanche gain and a bandwidth of 33 GHz [79]. As shown in Fig. 11(b), a strong electric field was generated in germanium by optimizing the silicon p-i-n junction with a p/n doping level of 10^{18} cm^{-3} and a 500 nm intrinsic silicon width. The impact ionization coefficient in germanium should have an order of magnitude higher than in silicon at the electric field of 0.2–0.4 MV/cm (Fig. 11(b)) [110, 111]. However, an effective k value as low as 0.2 was achieved, thanks to the dead space effect and the high electric field near the Si-Ge boundary [69, 71]. In addition, Benedikovic et al. proposed a heterostructure APD based on a lateral p-i-n structure as well, as illustrated in Fig. 11(c) [80]. Due to the simple APD scheme, photonic devices other than photodetectors, such as modulators, can be simultaneously fabricated. The APD exhibited a multiplication gain of 120, a GBP of 210 GHz, and an effective k of 0.25 without complex epitaxial structures and multiple ion implantation schemes. The study



of the APD multiplication gain versus the bias voltage under different input powers indicates that the multiplication gain increases with the decrease of the input optical power. The phenomenon also occurs in other types of APDs. The high input optical power results in a stronger space charge effect which hinders the impact ionization process. To study the effect of germanium geometry on device performance, Benedikovic et al. investigated a lateral p-i-n APD with various germanium widths and lengths, as shown in Fig. 11(d) [116]. High GBP up to 480 GHz and low k value down to 0.15 were achieved for APD with 0.3 μm width of germanium.

APD receivers

Performance metrics of state-of-the-art Si-Ge APDs discussed previously are summarized in order in Table 1. After converting an optical signal to an electrical signal by an APD, a following receiver circuitry is necessary to amplify, reshape, and process the electrical signal. Compared to a p-i-n photodiode, an APD require a more complex receiver due to the high bias voltage and various gains as a function of the bias voltage. An accurate APD model is beneficial to design a high-speed APD receiver [61–65]. Particularly, the performance of a TIA, such as bandwidth and input referred noise, is significantly affected by APDs. Wang et al. proposed an APD equivalent circuit model, including the effects of carrier transit time, avalanche buildup time and electrical parasitics, as shown in Fig. 12(a) [61]. This model can capture both electrical and optical dynamics over a wide range of multiplication gain. The space charge effect occurred at high gain region is described as a resistor R_a and an inductor L_a in series as shown at the absorption and avalanche region of the electrical parasitics in Fig. 12(a). $\omega_{RC} = \frac{1}{R_t C_t}$ and $Q = \frac{1}{R_t} \sqrt{\frac{L_t}{C_t}}$

Table 1 Performance metrics of state-of-the-art Si–Ge avalanche photodiode receivers

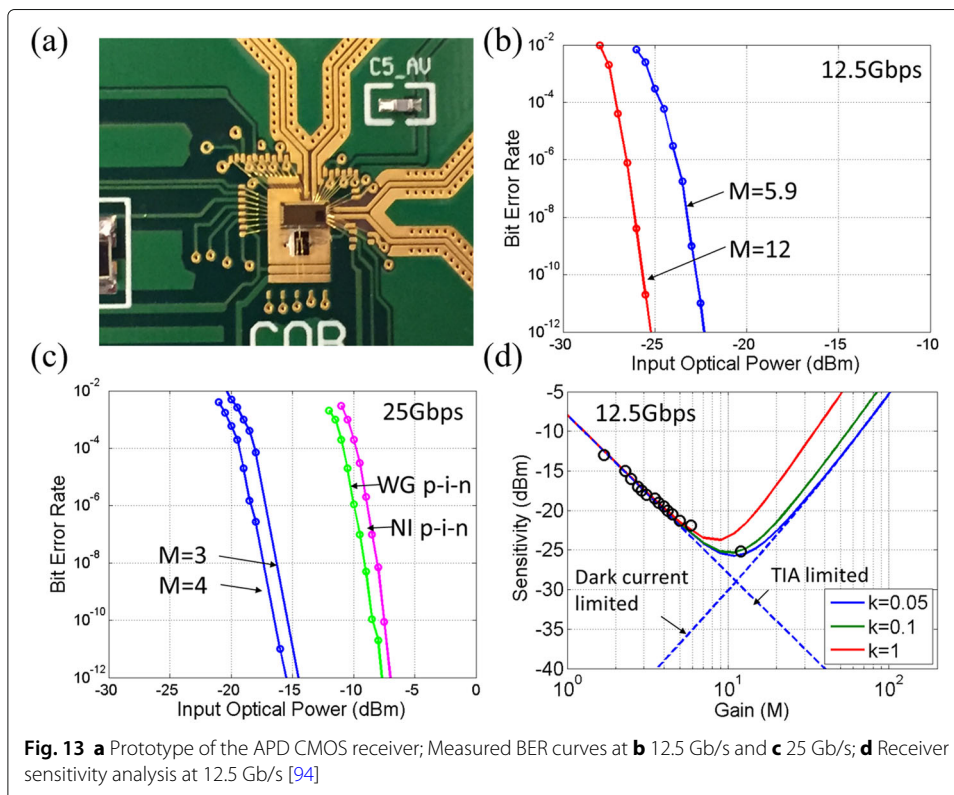
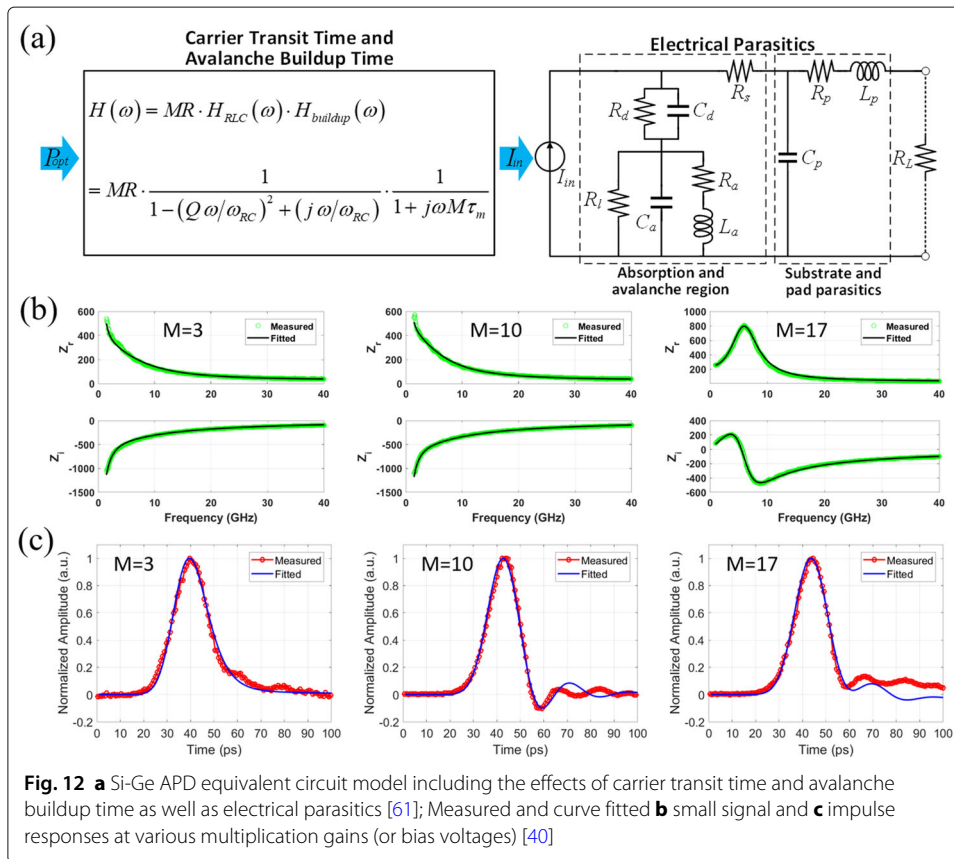
Ref.	$\lambda(\mu\text{m})$	$V_B(\text{V})$	k	GBP(GHz)	DR(Gbps)	Mod.	Sensitivity(dBm)
[72]	1.3	25	0.09	340	10	OOK	$-28@10^{-12}$
[86]	1.55	29.4	-	310	-	-	-
[87]	1.31	18	-	240	25	OOK	$-22.5@10^{-12}$
[88]	1.3/1.5	26.5	-	460	40	OOK	$-13.9@10^{-12}$
[89]	1.31	12	-	150	50	OOK	$-16@10^{-4}$
[73]	1.31	24	-	845	-	-	-
[74]	1.3/1.5	3.5	0.2	300	10	OOK	$-13.9@10^{-9}$
[93]	1.3	20	-	115	25	OOK	$-30.5@10^{-10}$
[94]	1.55	10	0.05	276	25	OOK	$-16@10^{-12}$
[95]	1.31	>18	-	360	-	-	-
[96]	1.31	>15	-	-	112	PAM4	$-8@10^{-4}$
[97]	1.55	6	-	400	28	OOK	$-9@10^{-12}$
[99]	1.31	16.5	-	260	106	PAM4	$-18@10^{-4}$
[40]	1.55	10	0.08	276	50	PAM4	$-16@10^{-4}$
[100]	1.55	10	-	500	64	PAM4	$-13@10^{-4}$
[101]	1.55	10	-	497	32	OOK	$-15.7@10^{-4}$
[105]	1.55	6	-	284	25	OOK	$-11.4@10^{-4}$
[107]	1.55	30.6	-	432	10	OOK	$-18.3@10^{-12}$
[109]	1.31	13	-	300	56	OOK	$-18.6@10^{-4}$
[112]	1.55	7	0.4	193	10	OOK	$-26@10^{-7}$
[113]	1.31	5	0.2	140	25	OOK	$-21.7@10^{-9}$
[114]	1.55	6.2	0.5	100	10	OOK	$-24.4@10^{-9}$
[79]	1.55	12.5	0.2	352	64	PAM4	$-3@10^{-6}$
[80]	1.55	11	0.25	210	40	OOK	$-11.2@10^{-9}$
[116]	1.55	16.5	0.15	480	80	OOK	$-13.3@10^{-9}$

in the RLC transfer function is related to bandwidth and damping. The buildup function describes the avalanche buildup process which limits the APD GBP, where τ_m is the avalanche buildup time, M is the multiplication gain, and $\tau_m = 1/(2\pi \times \text{GBP})$ [117–119]. Model parameters need to be set as a function of bias voltage or multiplication gain for the availability over a wide range of gain. These parameters can be extracted by curve fitting small-signal and impulse response characteristics, as shown in Fig. 12(b) and (c).

The main purpose of using APDs is to improve the receiver sensitivity. Hence, the APD receiver sensitivity analysis is necessary to design an APD for required system performance [40, 101, 109]. Generally, the bit error rate (BER) or Q-factor at a data rate is used to measure the performance of a transceiver, which can also be described as signal-to-noise ratio (SNR). The direct detection technology will be taken as an example to discuss below. The quality of a signal, i.e. Q-factor, is given by

$$Q = \frac{OMA \cdot R \cdot M}{\sigma_1 + \sigma_0} \quad (2)$$

where OMA is the effective optical modulation amplitude (OMA), R is the APD responsivity at unity gain, M is the APD multiplication gain, σ_1 and σ_0 are the receiver noise on level “1” and “0” [40]. The effective difference of two signal levels, OMA, is the eye height of a noiseless eye diagram at the receiver, which needs to count the eye degradation due to the intersymbol interference (ISI) [120, 121]. The bandwidth, the deterministic jitter, and



the nonlinear effect in a transceiver system contribute to the ISI. Here, the receiver sensitivity is analyzed using pulse amplitude modulation with two levels (PAM-2 or OOK) format for simplicity, which is also valid for advanced PAM-n ($n > 2$) modulation.

The total noise of an APD receiver on each signal level mainly consists of the laser relative intensity noise, the shot noise of photocurrent and dark current, and the TIA input referred noise, as described by

$$\sigma_{total} = \sqrt{\sigma_{RIN}^2 + \sigma_{shot}^2 + \sigma_{TIA}^2} \tag{3}$$

where

$$\sigma_{RIN}^2 = M^2 \cdot I_{photo}^2 \cdot RIN \cdot BW \tag{4}$$

$$\sigma_{shot}^2 = F \cdot M^2 \cdot 2q(I_{photo} + I_{dark}) \cdot BW \tag{5}$$

Here, M is the APD multiplication gain, I_{photo} is the photocurrent at unity gain, I_{dark} is the dark current at unity gain, RIN is the laser relative intensity noise, BW is the APD receiver bandwidth, and F is the APD excess noise factor [40]. The TIA input referred noise depends on the type of TIAs, which can refer to a TIA model [122].

Huang et al. demonstrated a waveguide-coupled Si-Ge vertical SACM APD integrated with a CMOS receiver circuit at 25 Gb/s whose prototype is shown in Fig. 13(a) [94]. The BER curves at different gains as well as the simulated and measured sensitivity data in Fig. 13 indicated that the APD receiver indeed improved the receiver sensitivity, thanks

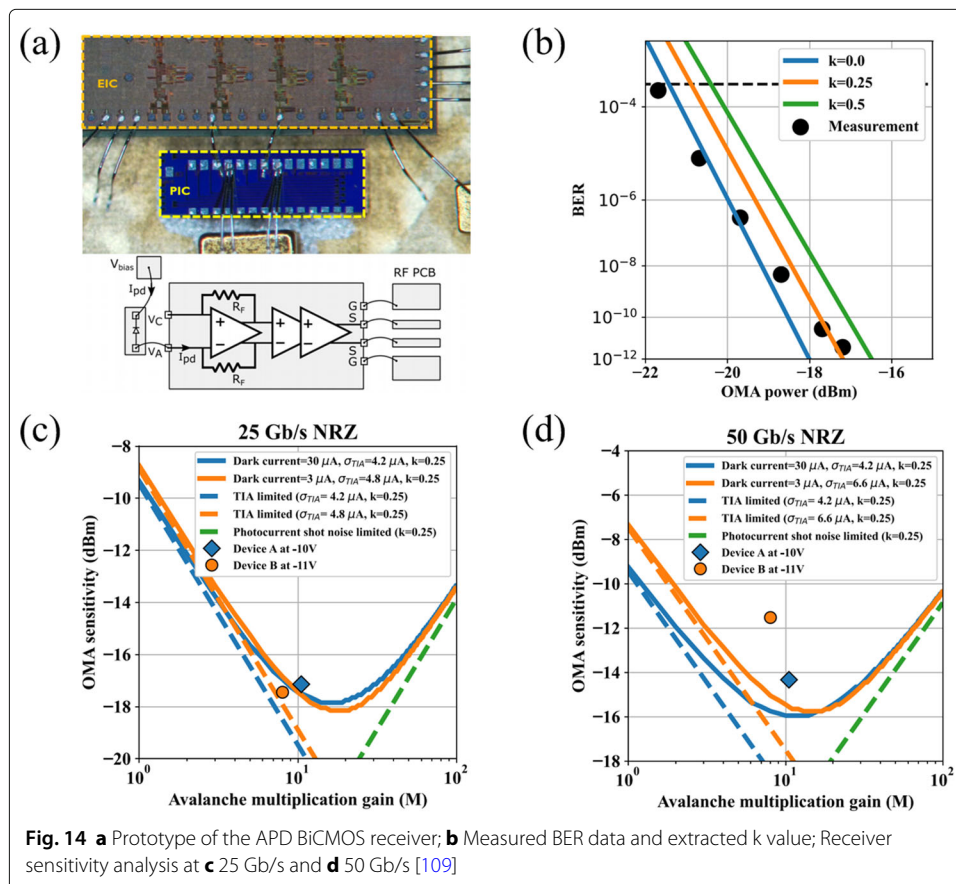


Fig. 14 **a** Prototype of the APD BiCMOS receiver; **b** Measured BER data and extracted k value; Receiver sensitivity analysis at **c** 25 Gb/s and **d** 50 Gb/s [109]

to the APD internal gain. The extracted k value was between 0.05 and 0.1. The optimum sensitivity was achieved around multiplication gain of 10. Additionally, Srinivasan et al. demonstrated a waveguide-coupled Si-Ge lateral SACM APD integrated with a BiCMOS receiver circuit at 56 Gb/s [109]. The APD receiver prototype and the BER and sensitivity results are shown in Fig. 14. The extracted k value was around 0.25. The high-speed APD receiver sensitivity analysis in [40, 94, 101, 109] concludes that the optimum sensitivity is realized at a multiplication gain range of 10-20 and the optimum gain depends on noise levels and data rates.

Conclusion

APD receivers with higher sensitivity are essential with the development of optical interconnect technologies towards higher bandwidth, higher integration, lower power consumption and lower cost. Si-Ge APDs with internal gain and low noise can greatly relax the requirements in link budget and power budget to realize higher bandwidth density. Important performance metrics for APD design include breakdown voltage, dark current, quantum efficiency, multiplication gain, bandwidth, excess noise, and GBP. Designing an APD with a low effective impact ionization coefficient ratio k is critical to realize high GBP and low noise. However, some design trade-offs may exist, which requires device optimization for different applications. How to break these trade-offs is one direction for future APD performance improvement. Si-Ge APD schemes can be optimized to trigger the impact ionization effect occurred in silicon more than that in germanium. The thickness of silicon or germanium can be thinned to increase the dead space effect, thereby reducing the k value. The consequent decreased responsivity or multiplication gain can be compensated by other methods, such as adding a reflector. The APD design also needs to consider the complexity and tolerance in device fabrication. Compared to vertical SACM APDs, APDs with lateral SACM or p-i-n structure can benefit from the less fabrication complexity but may require device processes with smaller linewidths. The overall noise sources have to be considered for optimizing APD receiver sensitivity. Design an APD with extremely high gain is not necessary for applications in high-speed optical interconnects since the optimum sensitivity for an APD receiver is achieved with a multiplication gain less than 20 in most cases.

Abbreviations

HPC: High performance computing; APD: Avalanche photodiode; GBP: Gain bandwidth product; Si-Ge: Silicon-germanium; SACM: Separate absorption charge multiplication; AI: Artificial intelligence; IoT: Internet of things; WDM: Wavelength division multiplexing; MDM: Mode division multiplexing; LIDAR: Light detection and ranging; CMOS: Complementary metal-oxide-semiconductor; LD: Laser diode; SOA: Semiconductor optical amplifier; PIC: Photonic integrated circuit; PDK: Process design kits; IC: Integrated circuit; PDF: Probability distribution function; MSM: Metal-semiconductor-metal; NI: Normal-incidence; NDR: Negative differential resistance; DBR: Distributed Bragg reflector; TIA: Transimpedance amplifier; MIM: Metal-insulator-metal; BER: Bit error rate; SNR: Signal-to-noise ratio; OMA: Optical modulation amplitude; PAM-n: Pulse amplitude modulation with n levels

Acknowledgements

Not applicable.

Authors' contributions

BW and JM conceived the manuscript. BW wrote the manuscript. JM revised the manuscript. BW and JM read and approved the final manuscript.

Funding

This work was supported by Shaanxi Province Overseas High-Level Talents Program, Chinese Academy of Sciences 100 Talents Program, Xi'an Institute of Optics and Precision Mechanics Start-Up Funding, and State Key Laboratory of Transient Optics and Photonics Independent Research Project.

Availability of data and materials

Data sharing is not applicable to this article as no datasets were generated or analysed during the current study.

Declarations

Competing interests

The authors declare that they have no competing interests.

Author details

¹State Key Laboratory of Transient Optics and Photonics, Xi'an Institute of Optics and Precision Mechanics, Chinese Academy of Sciences, Xi'an, China. ²University of Chinese Academy of Sciences, Beijing, China. ³Key Laboratory of Space Precision Measurement Technology, Xi'an Institute of Optics and Precision Mechanics, Chinese Academy of Sciences, Xi'an, China.

Received: 31 December 2021 Accepted: 9 March 2022

Published online: 25 March 2022

References

1. Ishio H, Minowa J, Nosu K. Review and status of wavelength-division-multiplexing technology and its application (invited overview). *J Light Technol.* 1984;2:448–63. <https://doi.org/10.1109/JLT.1984.1073653>.
2. Li H, Xuan Z, Titriku A, Li C, Yu K, Wang B, Shafik A, Qi N, Liu Y, Ding R, Baehr-Jones T, Fiorentino M, Hochberg M, Palermo S, Chiang PY. A 25 gb/s, 4.4 v-swing, ac-coupled ring modulator-based wdm transmitter with wavelength stabilization in 65 nm cmos. *IEEE J Solid State Circ.* 2015;50:3145–59. <https://doi.org/10.1109/JSSC.2015.2470524>.
3. Liang D, Roshan-Zamir A, Fan YH, Zhang C, Wang B, Descos A, Shen W, Yu K, Li C, Fan G, Kurczveil G, Hu Y, Huang Z, Fiorentino M, Kumar S, Palermo SM, Beausoleil RG. Fully-integrated heterogeneous dml transmitters for high-performance computing. *J Light Technol.* 2020;38:3322–37. <https://doi.org/10.1109/JLT.2019.2959048>.
4. Bozinovic N, Yue Y, Ren Y, Tur M, Kristensen P, Huang H, Willner AE, Ramachandran S. Terabit-scale orbital angular momentum mode division multiplexing in fibers. *Science.* 2013;340:1545–8. <https://doi.org/10.1126/science.1237861>.
5. Wu X, Huang C, Xu K, Shu C, Tsang HK. Mode-division multiplexing for silicon photonic network-on-chip. *J Lightwave Technol.* 2017;35:3223–8. <https://doi.org/10.1109/JLT.2017.2677085>.
6. Fazea Y, Mezhyuev V. Selective mode excitation techniques for mode-division multiplexing: A critical review. *Opt Fiber Technol.* 2018;45:280–8. <https://doi.org/10.1016/j.yofte.2018.08.004>.
7. Puttnam BJ, Rademacher G, Luis RS. Space-division multiplexing for optical fiber communications. *Optica.* 2021;8:1186. <https://doi.org/10.1364/optica.427631>.
8. Wang B, Huang Q, Chen K, Zhang J, Kurczveil G, Liang D, Palermo S, Tan MRT, Beausoleil RG, He S. Modulation on silicon for datacom: Past, present, and future. *Prog Electromagn Res.* 2019;166:119–45.
9. Bernabé S, Wilmar Q, Hasharoni K, Hassan K, Thonnart Y, Tissier P, Désières Y, Olivier S, Tekin T, Szelag B. Silicon photonics for terabit/s communication in data centers and exascale computers. *Solid State Electron.* 2021;179. <https://doi.org/10.1016/j.sse.2020.107928>.
10. Dumais P, Goodwill DJ, Celo D, Jiang J, Zhang C, Zhao F, Tu X, Zhang C, Yan S, He J, Li M, Liu W, Wei Y, Geng D, Mehruvar H, Bernier E. Silicon photonic switch subsystem with 900 monolithically integrated calibration photodiodes and 64-fiber package. *J Lightwave Technol.* 2018;36:233–8. <https://doi.org/10.1109/JLT.2017.2755578>.
11. Seok TJ, Kwon K, Henriksson J, Luo J, Wu MC. Wafer-scale silicon photonic switches beyond die size limit. *Optica.* 2019;6:490. <https://doi.org/10.1364/optica.6.000490>.
12. Shen Y, Harris NC, Skirlo S, Prabhu M, Baehr-Jones T, Hochberg M, Sun X, Zhao S, Larochelle H, Englund D, Soljacic M. Deep learning with coherent nanophotonic circuits. *Nat Photonics.* 2017;11:441–6. <https://doi.org/10.1038/nphoton.2017.93>.
13. Harris NC, Carolan J, Bunandar D, Prabhu M, Hochberg M, Baehr-Jones T, Fanto ML, Smith AM, Tison CC, Alsing PM, Englund D. Linear programmable nanophotonic processors. *Optica.* 2018;5:1623. <https://doi.org/10.1364/optica.5.001623>.
14. Sun J, Timurdogan E, Yaacobi A, Hosseini ES, Watts MR. Large-scale nanophotonic phased array. *Nature.* 2013;493:195–9. <https://doi.org/10.1038/nature11727>.
15. Martin A, Dodane D, Leviandier L, Dolfi D, Naughton A, O'Brien P, Spuessens T, Baets R, Lepage G, Verheyen P, Heyn PD, Absil P, Feneyrou P, Bourderionnet J. Photonic integrated circuit-based fmcw coherent lidar. *J Lightwave Technol.* 2018;36:4640–5. <https://doi.org/10.1109/JLT.2018.2840223>.
16. Wang Z, Yi S, Chen A, Zhou M, Luk TS, James A, Nogan J, Ross W, Joe G, Shahsafi A, Wang KX, Kats MA, Yu Z. Single-shot on-chip spectral sensors based on photonic crystal slabs. *Nat Commun.* 2019;10:3–8. <https://doi.org/10.1038/s41467-019-08994-5>.
17. Pohl D, Escalé MR, Madi M, Kaufmann F, Brotzer P, Sergeev A, Guldimmann B, Giaccari P, Alberti E, Meier U, Grange R. An integrated broadband spectrometer on thin-film lithium niobate. *Nat Photonics.* 2020;14:24–9. <https://doi.org/10.1038/s41566-019-0529-9>.
18. Lai YH, Suh MG, Lu YK, Shen B, Yang QF, Wang H, Li J, Lee SH, Yang KY, Vahala K. Earth rotation measured by a chip-scale ring laser gyroscope. *Nat Photonics.* 2020;14:345–9. <https://doi.org/10.1038/s41566-020-0588-y>.
19. Dong P, Chen YK, Duan GH, Neilson DT. Silicon photonic devices and integrated circuits. *Nanophotonics.* 2014;3:215–28. <https://doi.org/10.1515/nanoph-2013-0023>.
20. Su Y, Zhang Y, Qiu C, Guo X, Sun L. Silicon photonic platform for passive waveguide devices: Materials, fabrication, and applications. *Adv Mater Technol.* 2020;5:1–19. <https://doi.org/10.1002/admt.201901153>.
21. Li C, Zhang M, Xu H, Tan Y, Shi Y, Dai D. Subwavelength silicon photonics for on-chip mode-manipulation. *Photonix.* 2021;2. <https://doi.org/10.1186/s43074-021-00032-2>.

22. Reed GT, Mashanovich G, Gardes FY, Thomson DJ. Silicon optical modulators. *Nat Photonics*. 2010;4:518–26. <https://doi.org/10.1038/nphoton.2010.179>.
23. Benedikovic D, Vivot L, Aubin G, Hartmann J.-m., Amar F, Roux XL, Alonso-Ramos C, Cassan É, Marris-Morini D, Fédéli J-M, Boeuf F, Szlagel B, Vivien L. Silicon–germanium receivers for short-wave-infrared optoelectronics and communications. *Nanophotonics*. 2021;10:1059–79. <https://doi.org/10.1515/nanoph-2020-0547>.
24. Liang D, Roelkens G, Baets R, Bowers JE. Hybrid integrated platforms for silicon photonics. *Materials*. 2010;3:1782–802. <https://doi.org/10.3390/ma3031782>.
25. Liu AY, Srinivasan S, Norman J, Gossard AC, Bowers JE. Quantum dot lasers for silicon photonics. *Photonics Res*. 2015;3:1–9. <https://doi.org/10.1016/bs.semsem.2019.07.007>.
26. Chen S, Li W, Wu J, Jiang Q, Tang M, Shutts S, Elliott SN, Sobiesierski A, Seeds AJ, Ross I, Smowton PM, Liu H. Electrically pumped continuous-wave iii-v quantum dot lasers on silicon. *Nat Photonics*. 2016;10:307–11. <https://doi.org/10.1038/nphoton.2016.21>.
27. Wang Y, Chen S, Yu Y, Zhou L, Liu L, Yang C, Liao M, Tang M, Liu Z, Wu J, Li W, Ross I, Seeds AJ, Liu H, Yu S. Monolithic quantum-dot distributed feedback laser array on silicon. *Optica*. 2018;5:528. <https://doi.org/10.1364/optica.5.000528>.
28. Komljenovic T, Huang D, Pintos P, Tran MA, Davenport ML, Bowers JE. Photonic integrated circuits using heterogeneous integration on silicon. *Proc IEEE*. 2018;106:2246–57. <https://doi.org/10.1109/JPROC.2018.2864668>.
29. Jones R, Doussiere P, Driscoll JB, Lin W, Yu H, Akulova Y, Komljenovic T, Bowers JE. Heterogeneously integrated inp/silicon photonics: Fabricating fully functional transceivers. *IEEE Nanotechnol Mag*. 2019;13:17–26. <https://doi.org/10.1109/MNANO.2019.2891369>.
30. Norman JC, Jung D, Zhang Z, Wan Y, Liu S, Shang C, Herrick RW, Chow WW, Gossard AC, Bowers JE. A review of high-performance quantum dot lasers on silicon. *IEEE J Quantum Electron*. 2019;55:1–11. <https://doi.org/10.1109/JQE.2019.2901508>.
31. Liu W, Li M, Guzzon RS, Norberg EJ, Parker JS, Lu M, Coldren LA, Yao J. A fully reconfigurable photonic integrated signal processor. *Nat Photonics*. 2016;10:190–5. <https://doi.org/10.1038/nphoton.2015.281>.
32. Lopez DP. Programmable integrated silicon photonics waveguide meshes: Optimized designs and control algorithms. *IEEE J Sel Top Quant Electron*. 2020;26. <https://doi.org/10.1109/JSTQE.2019.2948048>.
33. Bogaerts W, Pérez D, Capmany J, Miller DAB, Poon J, Englund D, Morichetti F, Melloni A. Programmable photonic circuits. *Nature*. 2020;586:207–16. <https://doi.org/10.1038/s41586-020-2764-0>.
34. Sun C, Wade MT, Lee Y, Orcutt JS, Alloatti L, Georgas MS, Waterman AS, Shainline JM, Avizienis RR, Lin S, Moss BR, Kumar R, Pavanello F, Atabaki AH, Cook HM, Ou AJ, Leu JC, Chen YH, Asanović K, Ram RJ, Popović MA, Stojanović VM. Single-chip microprocessor that communicates directly using light. *Nature*. 2015;528:534–8. <https://doi.org/10.1038/nature16454>.
35. Atabaki AH, Moazeni S, Pavanello F, Gevorgyan H, Notaros J, Alloatti L, Wade MT, Sun C, Kruger SA, Meng H, Qubaisi KA, Wang I, Zhang B, Khilo A, Baiocco CV, Popović MA, Stojanović VM, Ram RJ. Integrating photonics with silicon nanoelectronics for the next generation of systems on a chip. *Nature*. 2018;556:349–53. <https://doi.org/10.1038/s41586-018-0028-z>.
36. Stojanović V, Ram RJ, Popović M, Lin S, Moazeni S, Wade M, Sun C, Alloatti L, Atabaki A, Pavanello F, Mehta N, Bhargava P. Monolithic silicon-photonic platforms in state-of-the-art cmos soi processes [invited]. *Opt Express*. 2018;26:13106. <https://doi.org/10.1364/oe.26.013106>.
37. Luan HC, Lim DR, Lee KK, Chen KM, Sandland JG, Wada K, Kimerling LC. High-quality ge epilayers on si with low threading-dislocation densities. *Appl Phys Lett*. 1999;75:2909–11. <https://doi.org/10.1063/1.125187>.
38. Hartmann JM, Damlencourt JF, Bogumilowicz Y, Holliger P, Rolland G, Billon T. Reduced pressure-chemical vapor deposition of intrinsic and doped ge layers on si(001) for microelectronics and optoelectronics purposes. *J Cryst Growth*. 2005;274:90–9. <https://doi.org/10.1016/j.jcrysgro.2004.10.042>.
39. Hartmann JM, Abbadie A, Cherkashin N, Grampeix H, Clavelier L. Epitaxial growth of ge thick layers on nominal and 6° off si(0 0 1); ge surface passivation by si. *Semicond Sci Technol*. 24;2009. <https://doi.org/10.1088/0268-1242/24/5/055002>.
40. Wang B, Huang Z, Sorin WW, Zeng X, Liang D, Fiorentino M, Beausoleil RG. A low-voltage si-ge avalanche photodiode for high-speed and energy efficient silicon photonic links. *J Lightwave Technol*. 2020;38:3156–63. <https://doi.org/10.1109/JLT.2019.2963292>.
41. Kumar A, Huang Z, Zeng X, Wang B, Liang D, Sorin W, Fiorentino M, Beausoleil RG, Palermo S. Design considerations for energy efficient dwdm pam4 transceivers employing avalanche photodiodes. *Laser Photonics Rev*. 2020;14. <https://doi.org/10.1002/lpor.202000142>.
42. Campbell JC. Recent advances in avalanche photodiodes. *J Lightwave Technol*. 2007;25:109–21. <https://doi.org/10.1364/ofc.1985.wc4>.
43. Campbell JC. Recent advances in avalanche photodiodes. *J Lightwave Technol*. 2016;34:12–4.
44. Huang M, Li S, Cai P, Hou G, Su Ti, Chen W, Hong CY, Pan D. Germanium on silicon avalanche photodiode. *IEEE J Sel Top Quant Electron*. 2018;24. <https://doi.org/10.1109/JSTQE.2017.2749958>.
45. Campbell J. Evolution of low-noise avalanche photodetectors. *IEEE J Sel Top Quant Electron*. 2022;28:1–11. <https://doi.org/10.1109/JSTQE.2021.3092963>.
46. McINTYRE RJ. Multiplication noise in uniform avalanche diodes. *IEEE Trans Electron Devices*. 1966;ED-13:164–8. <https://doi.org/10.1109/T-ED.1966.15651>.
47. Teich MC, Matsuo K, Saleh BEA. Excess noise factors for conventional and superlattice avalanche photodiodes and photomultiplier tubes. *IEEE J Quantum Electron*. 1986;22:1184–93. <https://doi.org/10.1109/JQE.1986.1073137>.
48. Lenox C, Nie H, Yuan P, Kinsey G, Homles AL, Streetman BG, Campbell JC. Resonant-cavity ingaas-inalas avalanche photodiodes with gain-bandwidth product of 290 ghz. *IEEE Photonics Technology Letters*. 1999;11:1162–4. <https://doi.org/10.1109/68.784238>.
49. Levine BF, Sacks RN, Ko J, Jazwiecki M, Valdmanis JA, Gunther D, Meier JH. A new planar ingaas-inalas avalanche photodiode. *IEEE Photon Technol Lett*. 2006;18:1898–900. <https://doi.org/10.1109/LPT.2006.881684>.

50. Wang S, Sidhu R, Zheng XG, Li X, Sun X, Holmes AL, Campbell JC. Low-noise avalanche photodiodes with graded impact-ionization-engineered multiplication region. *IEEE Photonics Technol Lett*. 2001;13:1346–8.
51. Wang S, Ma F, Li X, Sidhu R, Zheng XG, Sun X, Holmes AL, Campbell JC. Ultra-low noise avalanche photodiodes with a "centered-well" multiplication region. *IEEE J Quant Electron*. 2003;39:375–378. <https://doi.org/10.1109/JQE.2002.807183>.
52. Lee CA, Logan RA, Batdorf RL, Kleimack JJ, Wiegmann W. Ionization rates for holes and electrons in silicon. *Phys Rev*. 1964;134:761–73. <https://doi.org/10.1103/PhysRev.105.1246>.
53. Grant WN. Electron and hole ionization rates in epitaxial silicon at high electric fields. *Solid State Electron*. 1973;16:1189–203. [https://doi.org/10.1016/0038-1101\(73\)90147-0](https://doi.org/10.1016/0038-1101(73)90147-0).
54. Shawon MJ, Saxena V. Rapid simulation of photonic integrated circuits using verilog-a compact models. *IEEE Trans Circ Syst I Regular Pap*. 2020;67:3331–41. <https://doi.org/10.1109/TCSI.2020.2983303>.
55. Wang B, Sorin WW, Palermo S, Tan MRT. Comprehensive vertical-cavity surface-emitting laser model for optical interconnect transceiver circuit design. *Opt Eng*. 2016;55:126103. <https://doi.org/10.1117/1.oe.55.12.126103>.
56. Zhu K, Saxena V, Kuang W. Compact verilog-a modeling of silicon traveling-wave modulator for hybrid cmos photonic circuit design. *Midwest Symp Circ Syst*. 2014;6:15–8. <https://doi.org/10.1109/MWSCAS.2014.6908490>.
57. Wu R, Chen C-H, Fedeli J-M, Fournier M, Cheng K-T, Beausoleil RG. Compact models for carrier-injection silicon microring modulators. *Opt Express*. 2015;23:15545. <https://doi.org/10.1364/OE.23.015545>.
58. Wang B, Li C, Chen C-H, Yu K, Fiorentino M, Beausoleil RG, Palermo S. A compact verilog-a model of silicon carrier-injection ring modulators for optical interconnect transceiver circuit design. *J Lightwave Technol*. 2016;34:2996–3005.
59. Shin MJ, Ban Y, Yu B-M, Rhim J, Member S, Zimmermann L, Choi W-Y. Parametric characterization of self-heating in depletion-type si micro-ring modulators. *IEEE J Sel Top Quantum Electron*. 2016;22:116–22.
60. Shin M, Ban Y, Yu B-M, Kim M-H, Rhim J, Member S, Zimmermann L, Choi W-Y. A linear equivalent circuit model for depletion-type silicon microring modulators. *IEEE Trans Electron Devices*. 2017;64:1140–5.
61. Wang B, Huang Z, Zeng X, Sorin WW, Liang D, Fiorentino M, Beausoleil RG. A compact model for si-ge avalanche photodiodes over a wide range of multiplication gain. *J Lightwave Technol*. 2019;37:3229–35. <https://doi.org/10.1109/JLT.2019.2913179>.
62. Ahmed SZ, Ganguly S, Yuan Y, Zheng J, Tan Y, Campbell JC, Ghosh AW. A physics based multiscale compact model of p-i-n avalanche photodiodes. *J Lightwave Technol*. 2021;39:3591–8. <https://doi.org/10.1109/JLT.2021.3068265>.
63. Lee MJ, Kang HS, Choi WY. Equivalent circuit model for si avalanche photodetectors fabricated in standard cmos process. *IEEE Electron Device Lett*. 2008;29:1115–7. <https://doi.org/10.1109/LED.2008.2000717>.
64. Dai D, Chen H-W, Bowers JE, Kang Y, Morse M, Paniccia MJ. Equivalent circuit model of a Ge/Si avalanche photodiode. In: 2009 6th IEEE International Conference on Group IV Photonics. 2009. p. 13–15. <https://doi.org/10.1109/GROUP4.2009.5338304>.
65. Dai D, Rodwell MJW, Bowers JE, Kang Y, Morse M. Derivation of the small signal response and equivalent circuit model for a separate absorption and multiplication layer avalanche photodetector. *IEEE J Sel Top Quant Electron*. 2010;16:1328–36. <https://doi.org/10.1109/JSTQE.2009.2038497>.
66. Izhnin II, Lozovoy KA, Kokhanenko AP, Khomyakova KI, Douhan RMH, Dirko VV, Voitsekhovskii AV, Fitych OI, Akimenko NY. Single-photon avalanche diode detectors based on group iv materials. *Appl Nanosci (Switzerland)*. 2021. <https://doi.org/10.1007/s13204-021-01667-0>.
67. Tan CH, Clark JC, David JPR, Rees GJ, Plimmer SA, Tozer RC, Herbert DC, Robbins DJ, Leong WY, Newey J. Avalanche noise measurement in thin si p-i-n diodes. *Appl Phys Lett*. 2000;76:3926–8. <https://doi.org/10.1063/1.126823>.
68. Saleh MA, Hayat MM, Sotirelis PP, Holmes AL, Campbell JC, Saleh BEA, Teich MC. Impact-ionization and noise characteristics of thin iii-v avalanche photodiodes. *IEEE Trans Electron Devices*. 2001;48:2722–31. <https://doi.org/10.1109/16.974696>.
69. Hayat MM, Sargeant WL, Saleh BEA. Effect of dead space on gain and noise in si and gaas avalanche photodiodes. *IEEE J Quantum Electron*. 1992;28:1360–5. <https://doi.org/10.1109/3.135278>.
70. Rees GJ, David JPR. Nonlocal impact ionization and avalanche multiplication. *J Phys D Appl Phys*. 2010;43. <https://doi.org/10.1088/0022-3727/43/24/243001>.
71. Hayat MM, Kwon OH, Wang S, Campbell JC, Saleh BEA, Teich MC. Boundary effects on multiplication noise in thin heterostructure avalanche photodiodes: Theory and experiment. *IEEE Trans Electron Devices*. 2002;49:2114–23. <https://doi.org/10.1109/TED.2002.805573>.
72. Kang Y, Liu HD, Morse M, Paniccia MJ, Zadka M, Litski S, Sarid G, Pauchard A, Kuo YH, Chen HW, Zaoui WS, Bowers JE, Beling A, McIntosh DC, Zheng X, Campbell JC. Monolithic germanium/silicon avalanche photodiodes with 340ghz gain-bandwidth product. *Nat Photonics*. 2009;3:59–63. <https://doi.org/10.1038/nphoton.2008.247>.
73. Zaoui WS, Chen H-W, Bowers JE, Kang Y, Morse M, Paniccia MJ, Pauchard A, Campbell JC. Frequency response and bandwidth enhancement in ge/si avalanche photodiodes with over 840ghz gain-bandwidth-product. *Opt Express*. 2009;17:12641. <https://doi.org/10.1364/oe.17.012641>.
74. Assefa S, Xia F, Vlasov YA. Reinventing germanium avalanche photodetector for nanophotonic on-chip optical interconnects. *Nature*. 2010;464:80–4. <https://doi.org/10.1038/nature08813>.
75. Joo J, Kim S, Kim IG, Jang KS, Kim G. High-sensitivity 10gbps ge photoreceiver operating at $\lambda \sim 1.55 \mu\text{m}$. *Opt Express*. 2010;18:16474–9. <https://doi.org/10.1109/ECOC.2010.5621182>.
76. Ono H, Fujikata J, Noguchi M, Takahashi H, Shimura D, Yaegashi H, Sasaki H. Si photonics butt-coupled waveguide germanium avalanche photodiodes with lateral sam structures. 2019 Opt Fiber Commun Conf Exposition (OFC). 2019;Th2A.9:1–3.
77. Sugeta T, Urisu T, Sakata S, Mizushima Y. Metal-semiconductor-metal photodetector for high-speed optoelectronic circuits. *Jpn J Appl Phys*. 1980;19:459–64. <https://doi.org/10.7567/JJAPS.19S1.459>.
78. Soole JBD, Schumacher H. Ingaas metal-semiconductor-metal photodetectors for long wavelength optical communications. *IEEE J Quant Electron*. 1991;27:737–52. <https://doi.org/10.1109/3.81384>.

79. Zhang J, Kuo BP-P, Radic S. 64gb/s pam4 and 160gb/s 16qam modulation reception using a low-voltage si-ge waveguide-integrated apd. *Opt Express*. 2020;28:23266. <https://doi.org/10.1364/oe.396979>.
80. Benedikovic D, Viot L, Aubin G, Hartmann J-M, Amar F, Roux XL, Alonso-Ramos C, Cassan E, Marris-Morini D, Crozat P, Boeuf F, Fédéli J-M, Kopp C, Szelag B, Vivien L. 40 gbps heterostructure germanium avalanche photo receiver on a silicon chip. *Optica*. 2020;7:775. <https://doi.org/10.1364/optica.393537>.
81. Ando H, Kanbe H, Kimura T, Yamaoka T, Kaneda T. Characteristics of germanium avalanche photodiodes in the wavelength region of 1–1.6 μm . *IEEE J Quantum Electron*. 1978;14:804–9. <https://doi.org/10.1109/JQE.1978.1069698>.
82. Robbins VM, Wang T, Brennan KF, Hess K, Stillman GE. Electron and hole impact ionization coefficients in (100) and in (111) si. *J Appl Phys*. 1985;58:4614–7. <https://doi.org/10.1063/1.336229>.
83. Yeom K, Hincley JM, Singh J. Calculation of electron and hole impact ionization coefficients in sige alloys. *J Appl Phys*. 1996;80:6773–82. <https://doi.org/10.1063/1.363746>.
84. Lee J, Gutierrez-aitken AL, Li SH, Bhattacharya PK. Responsivity and impact ionization coefficients of $si_{1-x}ge_x$ photodiodes. *IEEE Trans Electron Devices*. 1996;43:977–81.
85. Yuan Y, Huang Z, Wang B, Sorin WW, Zeng X, Liang D, Fiorentino M, Campbell JC, Beausoleil RG. 64 gbps pam4 si-ge waveguide avalanche photodiodes with excellent temperature stability. *J Lightwave Technol*. 2020;38:4857–66. <https://doi.org/10.1109/JLT.2020.2996561>.
86. Duan N, Liow T-Y, Lim AE-J, Ding L, Lo GQ. 310 ghz gain-bandwidth product ge/si avalanche photodetector for 1550 nm light detection. *Opt Express*. 2012;20:11031. <https://doi.org/10.1364/oe.20.011031>.
87. Huang M, Cai P, Li S, Wang L, Su TI, Zhao L, Chen W, Hong CY, Pan D. Breakthrough of 25gb/s germanium on silicon avalanche photodiode. 2016 Opt Fiber Commun Conf Exhibition (OFC). 2016;M3A.3:1–3. <https://doi.org/10.1364/ofc.2016.tu2d.2>.
88. Kim G, Kim S, Kim SA, Oh JH, Jang K-S. Ndr-effect vertical-illumination-type ge-on-si avalanche photodetector. *Opt Lett*. 2018;43:5583–6.
89. Park S, Malinge Y, Dosunmu O, Lovell G, Slavin S, Magruder K, Kang Y, Liu A. 50-gbps receiver subsystem using ge/si avalanche photodiode and integrated bypass capacitor. 2019 Opt Fiber Commun Conf Exhibition (OFC). 2019;M3A.3:1–3.
90. Dai D, Chen H-W, Bowers JE, Kang Y, Morse M, Paniccia MJ. Resonant normal-incidence separate-absorption-charge-multiplication ge/si avalanche photodiodes. *Opt Express*. 2009;17:16549–57.
91. Bowers JE, Dai D, Zaoui WS, Kang Y, Morse M. Resonant si/ge avalanche photodiode with an ultrahigh gain bandwidth product. 2010 IEEE Photon Soc Winter Topicals Meet Ser (WTM). 2010;WC2.2:111–2.
92. Duan N, Liow TY, Lim AEJ, Ding L, Lo GQ. High speed waveguide-integrated ge/si avalanche photodetector. 2013 Optical Fiber Commun Conf Exposition (OFC). 2013;OM3K3:1–3. <https://doi.org/10.1364/ofc.2013.om3k.3>.
93. Liow TY, Duan N, Lim AEJ, Tu X, Yu M, Lo GQ. Waveguide ge/si avalanche photodetector with a unique low-height-profile device structure. 2014 Opt Fiber Commun Conf Exhibition (OFC). 2014;M2G.6:1–3. <https://doi.org/10.1364/ofc.2014.m2g.6>.
94. Huang Z, Li C, Liang D, Yu K, Santori C, Fiorentino M, Sorin W, Palermo S, Beausoleil RG. 25 gbps low-voltage waveguide si-ge avalanche photodiode. *Optica*. 2016;3:793. <https://doi.org/10.1364/optica.3.000793>.
95. Huang M, Cai P, Li S, Hou G, Zhang N, Su TI, Hong CY, Pan D. 56ghz waveguide ge/si avalanche photodiode. 2018 Opt Fiber Commun Conf Exposition (OFC). 2018;W4D.6:1–3.
96. Samani A, Carpentier O, El-Fiky E, Jacques M, Kumar A, Wang Y, Guenin L, Gamache C, Koh PC, Plant DV. Highly sensitive, 112 gb/s o-band waveguide coupled silicon-germanium avalanche photodetectors. 2019 Opt Fiber Commun Conf Exhibition (OFC). 2019;Th3B.1:1–3.
97. Carpentier O, Samani A, Jacques M, El-Fiky E, Alam MS, Wang Y, Koh PC, Calvo NA, Plant D. High gain-bandwidth waveguide coupled silicon germanium avalanche photodiode. 2020 Conf Lasers Electro-Optics (CLEO). 2020;STh4O.3:1–2. https://doi.org/10.1364/CLEO_SI.2020.STh4O.3.
98. Anthony R, Hagan DE, Genuth-Okon D, Maestro LM, Crowe IF, Halsall MP, Knights AP. Extended wavelength responsivity of a germanium photodetector integrated with a silicon waveguide exploiting the indirect transition. *IEEE J Sel Top Quantum Electron*. 2020;26:1–7. <https://doi.org/10.1109/JSTQE.2019.2938057>.
99. Huang M, Magruder K, Malinge Y, Fakhimi P, Liao H-H, Kohen D, Lovell G, Qian W, Lee K, Brandt C, Hakami M, Chen Y-J, Carabjal E, Guillermo E, Slavin S, Liu A. Recess-type waveguide integrated germanium on silicon avalanche photodiode; recess-type waveguide integrated germanium on silicon avalanche photodiode. 2021 Opt Fiber Commun Conf Exposition (OFC). 2021;F2C.3:1–3.
100. Wang B, Huang Z, Yuan Y, Liang D, Zeng X, Fiorentino M, Beausoleil RG. 64 gb/s low-voltage waveguide sige avalanche photodiodes with distributed bragg reflectors. *Photon Res*. 2020;8:1118. <https://doi.org/10.1364/prj.390339>.
101. Yuan Y, Huang Z, Zeng X, Liang D, Sorin WW, Fiorentino M, Beausoleil RG. High responsivity si-ge waveguide avalanche photodiodes enhanced by loop reflector. *IEEE J Sel Top Quantum Electron*. 2022;28:1–8. <https://doi.org/10.1109/JSTQE.2021.3087416>.
102. Wei J, Xu P, Wu H-P., Lee FC, Yao K, Ye M. Comparison of three topology candidates for 12 V VRM. In: APEC 2001. Sixteenth Annual IEEE Applied Power Electronics Conference and Exposition (Cat. No.01CH37181). 2001. p. 245–51. <https://doi.org/10.1109/APEC.2001.911655>.
103. Briere MA. Advanced power devices for many-core processor power supplies. *Tech Dig Int Electron Devices Meet IEDM*. 2010;328–31. <https://doi.org/10.1109/IEDM.2010.5703357>.
104. Ware M, Rajamani K, Floyd M, Brock B, Rubio JC, Rawson F, Carter JB. Architecting for power management: The IBM® POWER7 approach. In: HPCA - 16 2010 The Sixteenth International Symposium on High-Performance Computer Architecture. 2010. p. 1–11. <https://doi.org/10.1109/HPCA.2010.5416627>.
105. Zeng X, Huang Z, Wang B, Liang D, Fiorentino M, Beausoleil RG. Silicon-germanium avalanche photodiodes with direct control of electric field in charge multiplication region. *Optica*. 2019;6:772. <https://doi.org/10.1364/optica.6.000772>.

106. Jamil E, Hayat MM, Davids PS, Camacho RM. 3d avalanche multiplication in si-ge lateral avalanche photodiodes. *Adv Photon Counting Tech X*. 2016;9858:98580. <https://doi.org/10.1117/12.2225037>.
107. Martinez NJD, Derosé CT, Brock RW, Starbuck AL, Pomerene AT, Lentine AL, Trotter DC, Davids PS. High performance waveguide-coupled ge-on-si linear mode avalanche photodiodes. *Opt Express*. 2016;24:19072. <https://doi.org/10.1364/oe.24.019072>.
108. Srinivasan SA, Berciano M, Heyn PD, Lardenois S, Pantouvaki M, Campenhout JV. 27 ghz silicon-contacted waveguide-coupled ge/si avalanche photodiode. *J Lightwave Technol*. 2020;38:3044–50. <https://doi.org/10.1109/JLT.2020.2986923>.
109. Srinivasan SA, Lambrecht J, Guermendi D, Lardenois S, Berciano M, Absil P, Bauwelinck J, Yin X, Pantouvaki M, Campenhout JV. 56 gb/s nrz o-band hybrid bicmos-silicon photonics receiver using ge/si avalanche photodiode. *J Lightwave Technol*. 2021;39:1409–15. <https://doi.org/10.1109/JLT.2020.3038361>.
110. Decker DR, Dunn CN. Determination of germanium ionization coefficients from small-signal impatt diode characteristics. *IEEE Trans Electron Devices*. 1970;ED-17:290–9.
111. Overstraeten RV, Man HD. Measurement of the ionization rates in diffused silicon p-n junctions. *Solid State Electron*. 1970;13:583–608.
112. Virost L, Crozat P, Fédéli JM, Hartmann JM, Marris-Morini D, Cassan E, Boeuf F, Vivien L. Germanium avalanche receiver for low power interconnects. *Nat Commun*. 2014;5:3–8. <https://doi.org/10.1038/ncomms5957>.
113. Chen HT, Verbist J, Verheyen P, Heyn PD, Lepage G, Coster JD, Absil P, Moeneclaey B, Yin X, Bauwelinck J, Campenhout JV, Roelkens G. 25-gb/s 1310-nm optical receiver based on a sub-5-v waveguide-coupled germanium avalanche photodiode. *IEEE Photon J*. 2015;7. <https://doi.org/10.1109/JPHOT.2015.2460116>.
114. Chen HT, Verbist J, Verheyen P, Heyn PD, Lepage G, Coster JD, Absil P, Yin X, Bauwelinck J, Campenhout JV, Roelkens G. High sensitivity 10gb/s si photonic receiver based on a low-voltage waveguide-coupled ge avalanche photodetector. *Opt Express*. 2015;23:815. <https://doi.org/10.1364/oe.23.000815>.
115. Verbist J, Lambrecht J, Moeneclaey B, Campenhout JV, Yin X, Bauwelinck J, Roelkens G. 40-gb/s pam-4 transmission over a 40 km amplifier-less link using a sub-5v ge apd. *IEEE Photon Technol Lett*. 2017;29:2238–41. <https://doi.org/10.1109/LPT.2017.2757608>.
116. Benedikovic D, Virost L, Aubin G, Hartmann JM, Amar F, Roux XL, Alonso-Ramos C, Cassan E, Marris-Morini D, Boeuf F, Fedeli JM, Szelag B, Vivien L. Silicon-germanium avalanche receivers with fj/bit energy consumption. *IEEE J Sel Top Quantum Electron*. 2022;28:3802508. <https://doi.org/10.1109/JSTQE.2021.3112494>.
117. Lee CA, Batdorf RL, Wiegmann W, Kaminsky G. Time dependence of avalanche processes in silicon. *J Appl Phys*. 1967;38:2787–96. <https://doi.org/10.1063/1.1710004>.
118. Naqvi IM. Effects of time dependence of multiplication process on avalanche noise. *Solid State Electron*. 1973;16:19–28.
119. Hsieh HC, Sargeant W. Avalanche buildup time of an inp/ingaasp/ingaas apd at high gain. *IEEE J Quantum Electron*. 1989;25:2027–35.
120. Norimatsu S, Maruoka M. Accurate q-factor estimation of optically amplified. *IEEE/OSA J Lightwave Technol*. 2002;20:19–27.
121. Downie JD. Relationship of q penalty to eye-closure penalty for nrz and rz signals with signal-dependent noise. *IEEE/OSA J Lightwave Technol*. 2005;23:2031–8. <https://doi.org/10.1109/JLT.2005.849899>.
122. Sackinger E. On the noise optimum of fet broadband transimpedance amplifiers. *IEEE Trans Circ Syst I*. 2012;59:2881–9. <https://doi.org/10.1109/TCSI.2012.2206452>.

Publisher's Note

Springer Nature remains neutral with regard to jurisdictional claims in published maps and institutional affiliations.

Submit your manuscript to a SpringerOpen[®] journal and benefit from:

- Convenient online submission
- Rigorous peer review
- Open access: articles freely available online
- High visibility within the field
- Retaining the copyright to your article

Submit your next manuscript at ► [springeropen.com](https://www.springeropen.com)
